

Electrostatic Properties of the Mechanosensitive Channel of Small Conductance MscS

Marcos Sotomayor,^{*†} Trudy A. van der Straaten,[†] Umberto Ravaioli,[†] and Klaus Schulten^{*†}

^{*}Department of Physics, and [†]Beckman Institute for Advanced Science and Technology, University of Illinois at Urbana-Champaign, Urbana-Champaign, Illinois

ABSTRACT The mechanosensitive channel of small conductance (MscS) belongs to a family of membrane proteins that are gated in response to changes in membrane tension, thereby protecting the cell from hypo-osmotic shock. Here we report on passive ion transport simulations of MscS in a POPC bilayer using a coarse-grained particle-based description based on the Boltzmann transport Monte Carlo method. Single channel current-voltage curves are computed over hundreds of nanoseconds for channel conformations derived from all-atom molecular dynamics simulations reaching an overall simulation time of over 5 μ s. Channel conformations similar to that of the crystal structure exhibit low conductance, whereas conformations reached after opening the channel by means of steered molecular dynamics simulations match experimentally determined conductances. However, while experiments indicate a slight preference for anionic currents, the simulated channel strongly selects anions over cations and the direction of rectification at high voltages is opposite to what is observed in experiments. Three-dimensional maps of time-averaged ion distribution and equilibrium occupancy profiles constructed from trajectory data indicate separation of anions and cations inside and in the immediate vicinity of the large cytoplasmic domain of MscS, in accordance with earlier molecular dynamics simulations. This separation arises from the distribution of ionizable residues of MscS and suggests a specific, yet unknown, functional purpose.

INTRODUCTION

Mechanosensation relies on ion channels that open and close in response to stress conveyed through other proteinaceous structures of the cell or the cellular membrane itself (1–5). In bacteria, mechanosensitive channels have been proposed to act as safety valves preventing the cell from bursting upon osmotic shock (2,6–8). Two bacterial mechanosensitive channels have been cloned and crystallized: the mechanosensitive channel of large conductance, MscL (*Mycobacterium tuberculosis*) (9,10) and the mechanosensitive channel of small conductance MscS (*Escherichia coli*) (7,11). While the gating mechanism for MscL is fairly well understood and multiple experimental and theoretical studies have been performed on it (12–19), the voltage-modulated and stress-dependent gating mechanism of MscS remains controversial (11,20–25).

The crystal structure of MscS displays three transmembrane helices (labeled TM1, TM2, TM3A, and TM3B) forming a pore of radius ~ 3.3 Å, originally suggested to represent the open state of the channel (11) with a conductance of ~ 1 nS and a slight anionic selectivity as determined in patch-clamp experiments (2,23,26). However, subsequent computational studies suggested that the crystal structure is not completely open (20). In addition, an experimental characterization of MscS in spheroplasts (23) revealed voltage-independent activation and strong voltage-dependent inactivation (first reported in (27)). Moreover, the channel activity was found to depend strongly on the rate of pressure applied and the

crystal conformation was suggested to represent an inactive state (23). A conductance substate for MscS has been recently discovered through an optimized patch-clamp setup (28) and two different closed conformations of MscS have been proposed as well. Indeed, molecular dynamics simulations of the entire MscS structure revealed an asymmetric closure when the channel was relaxed in a POPC membrane for several nanoseconds (21) (also reported in (29)). On the other hand, a symmetric closed model was proposed based on Monte Carlo simulations and site-directed mutagenesis studies that characterize the role of the glycine-rich TM3A helix in MscS gating (22).

In addition to the transmembrane pore, MscS features a large cytoplasmic domain of unclear function with seven side openings and one distal pore. Recent studies have indirectly implicated this balloon-shaped domain in gating (30–32), desensitization and stability (33,34), as well as transport and selectivity (21). Specific interactions between the cytoplasmic domain and the transmembrane domain were implicated in MscS gating (21).

While the various studies mentioned above have shed light on architectural and functional properties of MscS, many questions remain unanswered and new ones have arisen: What is the actual physiological role of MscS, i.e., is MscS only a safety valve? Is the published structure significantly distorted due to crystallization conditions? Does the crystal structure show a so-called conductance substate, not a fully open state? What residues of MscS are relevant for its gating? What is the role of MscS's large cytoplasmic domain?

Molecular dynamics (MD) simulations provide a necessary complement to the experimental effort toward an answer to these questions. However, realistic simulations of a

Submitted December 20, 2005, and accepted for publication February 27, 2006.

M. Sotomayor and T. A. van der Straaten contributed equally to this article. Address reprint requests to Klaus Schulten, E-mail: kschulte@ks.uiuc.edu.

© 2006 by the Biophysical Society

0006-3495/06/05/3496/15 \$2.00

doi: 10.1529/biophysj.105.080069

complete channel embedded in a membrane environment present a formidable problem (35–38). Relevant cellular dimensions range from ~ 10 nm to ~ 1 mm, while specific channel behaviors, such as switching or selectivity, are also controlled by sub-nanometer functional subunits of the protein. In addition, strong short-range ion-ion and ion-protein interactions require ion dynamics to be resolved on a femtosecond timescale while reliable estimates of current require simulations lasting several 100 ns.

Although large-scale MD simulations provide detailed insight into the mechanisms of channel structure, gating, and selectivity (see (39) and references within), reliable estimates of channel conductance are barely possible with resources currently available (24,40). Continuum models based on Poisson-Nernst-Planck (Drift-Diffusion) theory have recently been proposed as a computationally efficient alternative means for computing channel conductances (41–54); however, the results of these models must be interpreted with caution, since the continuum paradigm deals with average densities rather than discrete particles of finite size, a premise that is problematic in channels only a few Angstroms wide (41,53). To extend simulation times well beyond the present limits of MD simulations, while still retaining the essential particle nature of the ions, a coarse-grained particle approach is needed. The Biology Monte Carlo (BioMOCA) ion channel simulator has been developed for this purpose (55), based on the Boltzmann transport Monte Carlo (56) and particle-particle-particle-mesh methodologies (57).

In this work we study the electrostatic properties of the crystal and various open conformations of MscS using a combined approach in which conformations obtained from MD are used as starting points for BioMOCA simulations, thus reaching timescales of hundreds of nanoseconds. The simulations revealed that ions permeate MscS through side openings of the cytoplasmic domain rather than the distal cytoplasmic pore; time-averaged electrostatic potential maps and ion densities reflect a strong localized separation of anions and cations inside and around the cytoplasmic domain and the transmembrane pore. We found that ionic currents computed for MscS conformations similar to those of the available crystal structure (11) were too small, while currents computed for wider conformations reached through steered MD simulations reproduce the experimentally determined values. However, ionic currents were found to be mainly driven by Cl^- ions, indicating a high selectivity for anions over cations, in relative disagreement with present experimental results that suggest slight anionic selectivity. Rectification at high voltages (>50 mV) was found to be in disagreement with experiments as well.

METHODS

The present work combines two different methodologies to explore the electrostatic properties of MscS, namely molecular dynamics (NAMD (58))

and a coarse-grained method (BioMOCA (55)). In this section we present first the protocols of all-atom molecular dynamics simulations used to generate MscS conformations. Simplified models of channels with different charge distributions are described as well. Then, details and parameters used in BioMOCA simulations of these conformations and models are described along with the diagnostics utilized.

MscS conformations from molecular dynamics simulations

Four different conformations of MscS obtained from molecular dynamics simulations were utilized for BioMOCA simulations (see below). In all molecular dynamics simulations, the crystal structure of MscS (Protein Data Bank code 1MXM (11)) was embedded in a membrane bilayer of 299 POPC lipids solvated with over 50,000 explicit water molecules (TIP3P) and 200 mM of KCl. The simulated system included altogether 224,340 atoms. The first conformation, referred to as *crystal*, was obtained after ~ 4.5 ns of dynamics with the backbone atoms of the protein restrained to their original positions in the crystal ($k = 1$ Kcal/mol/Å²), but all other atoms free to equilibrate otherwise (Fig. 1, A and B; and Supplementary Material's Fig. 7 A). This *crystal* conformation features a pore slightly narrower than that of the crystal itself ($r_{\text{min}} = 2.8$ Å compared to 3.3 Å; all pore radii were computed using HOLE (59) and default AMBER van der Waals radii for consistency with previous work, see (21) for details). The second conformation, labeled *open1*, was obtained after ~ 4.6 ns of dynamics in which restraints to backbone atoms were gradually released while a surface tension of 20 dyne/cm was applied to the system (Fig. 1 C and Supplementary Material's Fig. 7 B). Details of the corresponding molecular dynamics simulations leading to *crystal* and *open1* conformations can be found in Sotomayor and Schulten (21).

Two additional MD simulations leading to *open2* and *open3* conformations were performed. Both simulations used conformation *open1* as a starting point (end of sim2b in (21)). During the first MD simulation, a surface tension of 50 dyne/cm was applied to the system in the plane of the membrane (x,y -plane; see (13,21)) along with a constant force of 10 pN acting on each of the C_α atoms of residues Tyr²⁷, Val²⁹, Arg⁴⁶, Arg⁵⁴, Arg⁵⁹, Arg⁷⁴, and Arg¹²⁸. Forces were applied radially, pointing outwards from the center of the channel, in the x,y -plane, for 12 ns (Supplementary Material's Fig. 7, E and F), after which the forces were increased to 40 pN and the system was simulated for an additional 4 ns, leading to conformation *open2* (Fig. 1 E and Supplementary Material's Fig. 7 C). The position of the center of the channel, used to define the direction of the forces applied, was updated at simulation times 4.5, 6.2, 9, 10.8, 12, 13.7, and 15 ns. The magnitude of the forces is comparable to those used previously to open MscL under similar conditions (18).

The second MD simulation, leading to conformation *open3* (Fig. 1 F), consisted of 1 ns of dynamics with an applied surface tension of 20 dyne/cm, followed by 1 ns of dynamics with an applied surface tension of 40 dyne/cm. Then, the surface tension was turned off, a constant volume protocol was assumed, and a force of 10 pN was applied to each of the C_α atoms of residues 96–113 (TM3B helix) over 1 ns (Supplementary Material's Fig. 7, G and H). Forces were then increased to 20 pN and the simulation continued for an additional 2 ns. Forces were applied radially in the x,y -plane pointing outwards from the center of the channel to induce contacts between TM1–TM2 and TM3, as loss of these contacts has been suggested to cause inactivation (23). All external forces were applied through the NAMD/Tcl interface (58).

Conformations *crystal*, *open1*, *open2*, and *open3* were taken from the last frame of the corresponding simulations described above and mapped to a rectilinear grid (see below) including protein and lipids, but not solvent and ions. Explicit lipids provide a more realistic, irregular membrane, leaving some space between crevices formed at the cytoplasmic side of the protein for ions to visit. Mobile water molecules within the bilayer are known to contribute to the membrane potential (60), but it is not clear how to best

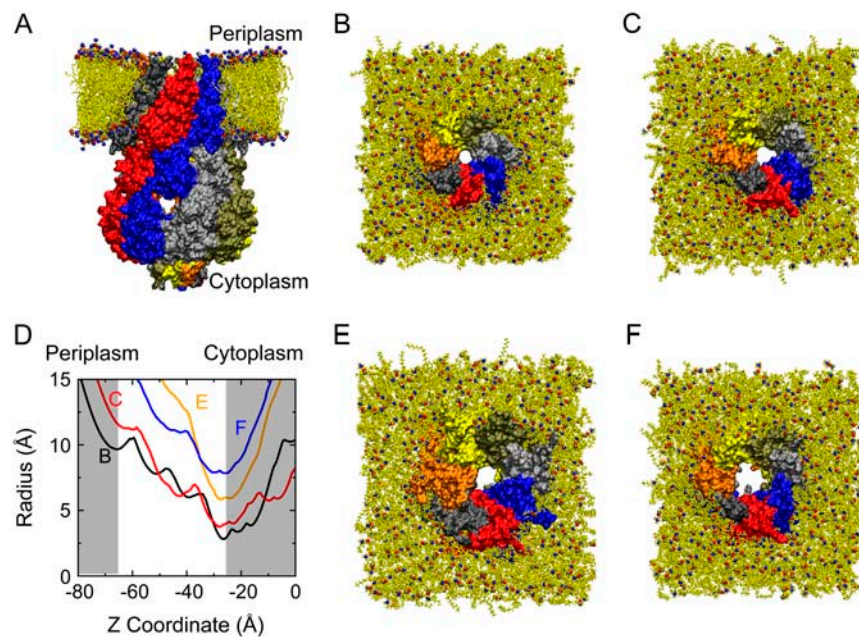


FIGURE 1 Conformations of MscS obtained through molecular dynamics simulations. (A) Side view of MscS embedded in a solvated POPC membrane bilayer ($\sim 225,000$ -atom system, water and ions not shown) after 4.5 ns of equilibration with its backbone restrained (21). The protein is shown in surface representation and each subunit is colored differently. Lipids are shown in yellow licorice representation while oxygen and nitrogen headgroup atoms are shown as red and blue spheres, respectively. (B) Top view of MscS conformation as shown in panel A, referred to as *crystal* throughout the text. (C) Top view of MscS's *open1* conformation obtained through a MD simulation in which backbone restraints were gradually released while surface tension was applied to the system (21) (4.6 ns, 20 dyne/cm). (D) Pore radius profile, as determined by HOLE (59), along the z axis for conformations *crystal* (black, $r_{\min} = 2.8$ Å), *open1* (red, $r_{\min} = 3.75$ Å), *open2* (blue, $r_{\min} = 5.8$ Å), and *open3* (yellow, $r_{\min} = 7.85$ Å). (E) Top view of MscS conformation *open2* obtained through a MD simulation in which surface tension was applied to the system along with forces acting on peripheral residues of MscS transmembrane domains (see

text). (F) Top view of MscS conformation *open3* obtained through a MD simulation in which forces were applied to residues lining the pore (TM3A helix; see text).

include them in the present context. A fourth conformation labeled *crystalNC* was obtained from *crystal* by excluding the cytoplasmic domain of MscS (residues 129–280). The mapping of each of the five conformations mentioned above (*crystal*, *open1*, *open2*, *open3* and *crystalNC*) was performed using the standard set of partial charges of CHARMM (61) along with a standard set of radii for atoms used in VMD (see Supplementary Material's Table 3). We decided not to use the standard set of CHARMM radii, since they have not been designed for continuum simulations (see (51,62–64) for examples in which atomic radii have been optimized for continuum simulations). Indeed, the combined sets of CHARMM charges and VMD radii are very similar to those of parameters for solvation energy (i.e., PARSE (65)), previously used for estimation of currents with continuum models. However, to assess the effect of this choice, a sixth conformation, labeled *crystalCR*, was constructed identical to *crystal* but using the standard set of CHARMM radii during the mapping to a rectilinear grid.

Schematic models

Four schematic models, referred to as *mod1*, *mod2*, *mod3*, and *mod4*, were built containing a slab of membrane of thickness 50 Å with a cylindrical pore of radius 5 Å. Each model featured three rings of seven atoms each ($r_{\text{atom}} = 1.5$ Å, unless otherwise stated). The first two rings were located at the cytoplasmic and periplasmic ends of the pore. The third ring was located 15 Å away from the membrane in the cytoplasmic bath. All rings were set neutral for *mod1*, whereas the rings at both ends of the channel were set positive and the third ring was set neutral for *mod2*. Model *mod3* featured positively charged rings at the ends of the channel while its third ring was negatively charged. The fourth model, *mod4*, designed as a control model, included two negatively charged rings at the ends of the channel and a third, neutral, ring.

Three additional schematic models (*mod5*, *mod6*, and *mod7*) with pores of radius 10 Å were prepared for BioMOCA simulations as well. Model *mod5* was decorated with three neutral rings of seven atoms each, as described above. Model *mod6* featured positively charged rings at the ends of the channel and a third, neutral, ring located 15 Å away from the membrane in the cytoplasmic bath. Finally, model *mod7* featured only two, neutral, rings at the ends of the channel.

Coarse-grained, particle-based simulations

Calculations of the electrostatic field around MscS and the current through its pore were carried out using the program BioMOCA; since the program has been described extensively elsewhere (55), we provide only a brief description here. In contrast to MD simulations, where the motion of every particle is explicitly resolved, in BioMOCA the protein, lipid, and water molecules are treated as static continuum dielectric media and only the trajectories of the mobile ions in solution are computed. This reduces the number of particles from $O(10^5)$ to $O(10^2)$, allowing much longer simulation times than what can currently be achieved using MD.

The molecular structures were taken from snapshots of molecular dynamics simulations or schematic models as described above, and mapped onto a rectilinear grid using the scheme implemented in the adaptive Poisson Boltzmann Solver (66), thus partitioning the simulation domain into three contiguous regions: protein, lipid, and electrolyte. For all of the simulations discussed here, a uniform grid with a mesh spacing of 1.5 Å was used. Probe radii of 1.38 Å and 4 Å were utilized to determine the protein and lipid boundaries, respectively.

Ion trajectories were computed in real space as sequences of free flights which are randomly interrupted by scattering events. This is equivalent to solving (with the Monte Carlo methodology) the Boltzmann Transport equation, widely used in solid-state physics to describe transport of electrons (57,67). The flight times t_f between scattering events were generated statistically from the total scattering rate for all scattering processes $\lambda_{\text{tot}}(\vec{p}(t))$, according to

$$-\ln(r) = \int_0^{t_f} \lambda_{\text{tot}}(\vec{p}(t)) dt, \quad (1)$$

where r is a random number uniformly distributed on the unit interval. In general, the scattering rate $\lambda_{\text{tot}}(\vec{p}(t))$ depends on the particle momentum \vec{p} , which in turn will depend on the ion's local environment, and constitutes the sum of individual scattering rates for various scattering processes (in the context of solid-state physics, any impurities, crystal defects, or thermal vibrations of the crystal lattice would be classified as different scattering processes). When an ion reaches the end of its free flight, another random

number is used to select which type of scattering event took place and the final state of the ion is selected according to the particular scattering model implemented. In regions of restricted volume, such as the interior of the channel pore, ion-water scattering processes are likely to be significantly different from bulk electrolyte processes and additional scattering processes may prevail. BioMOCA has been, therefore, equipped to handle multiple scattering processes, and space- and momentum-dependent scattering rates. However, in this study we have assumed a single scattering mechanism that thermalizes the ions, with a constant scattering rate λ_i for each species, linked to an ion's mass m_i , and diffusion coefficient D_i in water,

$$\lambda_i = \frac{k_B T}{m_i D_i}, \quad (2)$$

where i denotes the ion label. For KCl transport we used the published K^+ and Cl^- diffusion coefficients measured in bulk electrolyte, e.g., $D_K = 1.957e-9 \text{ m}^2 \text{ s}^{-1}$ and $D_{Cl} = 2.032e-9 \text{ m}^2 \text{ s}^{-1}$ (68), yielding scattering rates of $\lambda_K = 3.26e13 \text{ s}^{-1}$ and $\lambda_{Cl} = 3.46e13 \text{ s}^{-1}$. At the end of each free flight the ion's velocity was reselected randomly from a Maxwellian distribution. The assumption of a single constant scattering rate yields ion transport that is equivalent to Brownian dynamics.

The use of a bulk-like, uniform diffusion coefficient for K^+ and Cl^- will likely result in the overestimation of computed currents for the narrower structures. Indeed, previous studies using all-atom MD simulations and hydrodynamic theory have shown that ion mobility is highly reduced in narrow channels (51,54,69). This effect seems to be similar for both K^+ and Cl^- ions and, therefore, should not affect selectivity (70). While the reduction in mobility should not be dramatic for a fully conductive channel with a large conductance like MscS, future studies should use position-dependent diffusion coefficients computed from all-atom MD simulations for MscS's transmembrane pore and all openings of its cytoplasmic domain.

Ion dynamics and field solution

In between scattering events, the ions moved in the electrolyte according to Newton's laws of motion in response to the local field. Trajectories were synchronously propagated in time and space by integrating the equations of motion using the second-order accurate leapfrog scheme (57). High ion-water scattering rates necessitated a short trajectory integration timestep of 10 fs. The total force on the ion was the sum of a pairwise ion-ion repulsive component, which represents ionic core repulsion, and an electrostatic component, which was obtained self-consistently by solving Poisson's equation,

$$\nabla \cdot \epsilon(\vec{r}) \nabla \phi(\vec{r}) = -[\rho_{\text{ions}}(\vec{r}) + \rho_{\text{perm}}(\vec{r})], \quad (3)$$

where $\phi(\vec{r})$ is the local electrostatic potential, $\rho_{\text{ions}}(\vec{r})$ and $\rho_{\text{perm}}(\vec{r})$ are, respectively, the densities of mobile ions and permanent fixed charge on the protein and lipids, and $\epsilon(\vec{r})$ is the local dielectric constant discussed below. Solving Eq. 3 over the entire domain subject to specific Dirichlet boundary conditions provided a simple way to include an applied bias and the effects of image charges induced at dielectric boundaries. The mobile charge density $\rho_{\text{ions}}(\vec{r})$ was recomputed from the positions of all ions in the system every 100 ion trajectory time steps, i.e., every 1 ps, as well as each time an ion entered or left the system, i.e., every time the total charge in the system changed. Each ion's charge was mapped to a finite rectilinear grid using the cloud-in-cell scheme (57) to weight the charge to the eight nearest grid points. The same procedure was used to map the fixed partial charges residing on the protein and lipid to the grid at the start of the simulation. Equation 3 was discretized using finite differences and solved using conjugate gradient (71) methods, subject to specific boundary conditions described below. Once the potential was known, the electrostatic field \vec{E}^{mesh} at each grid point was obtained using second-order finite differences and the field at the eight nearest grid points was then weighted back to the ion using the same interpolation kernel as was used to map the charge density. Discretization of Poisson's equation leads to an unavoidable truncation of the short-range component of the electrostatic force, which was corrected

using the particle-particle-particle-mesh scheme (55,57). A pairwise force which prevents ions from coalescing unphysically was also included as mentioned above. For computational efficiency we implemented a truncated-shifted form of the Lennard-Jones 6-12 potential that retains only the short-range repulsive component (55). We note, however, that the parameters describing pairwise interactions do not take into account the effect of missing water molecules with a finite volume (hydration shells), and have not been validated against known activity coefficients.

The protein and lipid regions were deemed inaccessible to ions by assigning a finite radius, equal to the Pauling ionic radius (72), to each ion. For K^+ and Cl^- ions these ionic radii are 1.33 Å and 1.81 Å, respectively. If any point within the spherical ion overlapped the protein or membrane boundary during a time-step, the ion was returned to its position at the beginning of the time-step and reflected diffusively. This process was repeated until the ion's final position lay outside the protein/membrane region.

Dielectric coefficients

Perhaps the most challenging aspect of coarse-grained ion channel simulations is the assignment of appropriate values for the protein, lipid, and electrolyte dielectric coefficients, which determine the strength of the electrostatic interaction between two charged species as well as the self-force felt by an ion as it approaches a dielectric boundary. The protein environment responds to external fields in several ways, each with its own relaxation timescale. For models that include the permanent protein dipoles explicitly, but treat the protein and water reorganization implicitly, the dielectric coefficient is hard to define, particularly when ion motion takes place on the same timescale as the protein's response to its presence. In such cases it has been suggested that the value of the protein dielectric coefficient depends on the nature of the interaction: for charge-dipole interactions a value between 4 and 6 is recommended, while for charge-charge interactions the protein dielectric coefficient can be >10 (73). For this work we kept $\epsilon_i = 2$ in the lipid region and used $\epsilon_p = 5$ in the protein region, unless stated otherwise. The electrolyte bath regions were assigned the dielectric coefficient of bulk water; e.g., $\epsilon_w \approx 80$. Note, however, that in most ion channels the pore is very narrow and is often lined with highly charged residues and/or strong permanent dipoles. As a result, water molecules can be highly ordered within the channel pore, restricting their response to external fields (74,75) and the dielectric coefficient ϵ_{ch} is likely to be $\ll 80$ and anisotropic. Although the transmembrane pore of MscS is wide enough to accommodate a few files of water molecules, all-atom MD simulations of MscS have shown intermittent permeation of water through the pore, or so-called dewetting transitions (20,21), which may also affect the dielectric properties of this region.

Ideally, the dielectric coefficient should decrease gradually from the bulk-like bath regions to the channel pore, but computing electrostatic forces acting on ions in regions surrounding a sharp transition in dielectric coefficient poses additional numerical complications. For the simulations presented here we have adopted the same approach as several other groups (51,64,76–78) and used $\epsilon_{\text{ch}} = 80$ inside the channel pore as well as in the electrolyte bath regions. However, we note that future studies should further investigate the value of the dielectric constant within the cytoplasmic domain of MscS and along its transmembrane pore.

Boundary conditions

Experimentally, the electrical properties of a single ion channel can be measured by inserting the channel into a lipid bilayer (membrane) separating two baths containing solutions of specific concentrations (79). Electrodes are immersed in the baths to maintain a constant bias voltage across the membrane. To adequately represent these contact regions without the computational overhead of including extremely large baths, we assumed that beyond a Debye length from the membrane surface the average electrostatic potential and ion densities do not vary appreciably, an assumption supported by the results of recent continuum simulations (80). For salt concentrations

considered here, this distance is of the order of 10 Å. Therefore, we imposed Dirichlet boundary conditions on the potential at the two domain boundary planes that lie parallel to the membrane, which are located ~15 Å from the periplasmic side of the lipid and 15 Å from the distal end of the cytoplasmic domain of the protein. Homogeneous, i.e., zero-field, Neumann boundary conditions were imposed at all other domain boundaries.

Electrolyte baths of fixed concentration were modeled on either side of the membrane as follows: Ions that left the domain through the Dirichlet boundary planes were removed from the simulation. If the ion population for each species in either bath fell below the value representing the desired density, new ions were injected with a Maxwellian velocity to maintain the given density. The newly injected ions were placed randomly within a 4 Å (6.25 Å for simplified models) slab from the Dirichlet boundary planes. It should be noted, however, that ions were never artificially removed from these buffer regions. Ions that attempted to cross the Neumann boundary planes were reflected elastically.

Calculation of potential maps, ion concentrations, and currents

Ionic currents were computed by counting the number of ions that crossed the membrane during the simulation and normalizing by the simulation duration (see (40,81) for alternative methods). For smaller channels like gramicidin this is an unambiguous means of estimating stationary current. For MscS, however, the number of ions that cross the membrane may not be an accurate measure of the actual experimental current since MscS's large cytoplasmic domain may lead to substantial, partial transport across the simulation volume. Nevertheless, trajectory analysis indicated that ions passed through the transmembrane pore relatively quickly ($O(100\text{ ps})$) and entered or left the cytoplasmic domain through its side openings within the simulation timescale used, i.e., partial transport was rare.

In addition to ionic currents, time-averaged three-dimensional maps of the electrostatic potential and ion concentrations were computed. Every time the Poisson equation was solved, the instantaneous ion density was sampled and added to a running average. One-dimensional average ion concentration $\bar{n}(k)$ plots were computed from the final concentration map by integrating the ion density $n(i, j, k)$ in the plane parallel to the Dirichlet, i.e., x,y -boundary planes, and normalizing by the total ion-accessible volume in that plane. For this purpose we employed the expression

$$\bar{n}(k) = \frac{\sum_i \sum_j n(i, j, k)}{\sum_i \sum_j N_{\text{H}_2\text{O}}(i, j, k)}, \quad (4)$$

where indices i, j , and k denote voxel labels in the x, y , and z directions, respectively, and where $N_{\text{H}_2\text{O}}(i, j, k)$ is 0 if voxel i, j, k belongs to a protein or lipid region, and 1 if voxel i, j, k belongs to a water region. One-dimensional occupancy $O(k)$ plots were computed by integrating the ion density $n(i, j, k)$ per 1.5 Å slab parallel to the membrane using

$$O(k) = \sum_i \sum_j (n(i, j, k) \Delta^3 C), \quad (5)$$

where $\Delta^3 = (1.5 \text{ Å})^3$ and $C = 6.022 \times 10^{26}$.

RESULTS AND DISCUSSION

The following sections describe electrostatic and transport properties of different MscS conformations and schematic models as determined through our MD and BioMOCA simulations. These descriptions are followed by an analysis of the effect of different approximations and sources of errors.

Electrostatic and transport properties of MscS in the *crystal* conformation

Four independent BioMOCA simulations of the *crystal* conformation of MscS were carried out (100 ns each) for symmetric baths of 0.1 M KCl and zero bias potential (0 voltage, see Table 1). Representative snapshots of the time-averaged electrostatic potential as well as the density of negative and positive ions are shown in Fig. 2. The distribution of ions shows a clear pattern with negative ions found mainly in and around the transmembrane pore of MscS and around the distal C-termini (Fig. 2, *B* and *E*). On the other hand, positive ions localize in and around the distal zone of the cytoplasmic domain (Fig. 2, *A* and *E*). The ionic density is particularly high around some regions of the cytoplasmic domain (Asp^{195,197,199,262}, Arg^{128,131}, and Lys¹⁶⁹) that may serve as binding spots for charged species (see Fig. 2 *A* for positive ions and Fig. 2 *B* for negative ions). The averaged electrostatic potential follows the corresponding trend: positive at the transmembrane region of MscS and the distal C-termini, negative at the distal zone of the cytoplasmic domain (Fig. 3 *A*). Spontaneous diffusion of ions through the transmembrane pore (crossings in Table 1) was monitored during these four simulations. The net current was approximately zero in all cases, as expected since the applied voltage was set to zero. However, only Cl⁻ ions crossed the transmembrane pore, whereas positive ions did not cross in either direction, indicating strong selectivity for anions over cations.

Electrostatic potential and ionic currents were also computed for six BioMOCA simulations of the *crystal* conformation, now using biasing potentials of ± 100 mV (see Table 1). Each simulation lasted 100 ns and was performed using a symmetric bath of 0.1 M KCl. The electrostatic potential and ion densities were found to follow the same general trend described above for equilibrium simulations (0 voltage, see Fig. 3 *B*). The ionic current through the transmembrane pore ($r_{\text{min}} = 2.8 \text{ Å}$, see Fig. 1, *B* and *D*) was found to be 41.7 ± 4.5 pA when the applied potential was set to 100 mV, and -13.9 ± 2 pA when the applied potential was set to -100 mV. In all cases, currents were almost exclusively driven by Cl⁻ ions (see Table 1). Two additional simulations using biasing potentials of ± 200 mV showed increased selectivity for anions over cations and higher currents for positive driving potentials (126.6 pA compared to -20.8 pA). Further BioMOCA simulations of the *crystal* conformation using symmetric baths of 0.2 M KCl at 0, ± 50 , and ± 100 mV showed similar results with high selectivity for anions over cations as well as higher currents for positive driving potentials. The rectification at negative potentials observed in the simulations is in disagreement with experimental results (2,23,26), but the electrostatic pattern and distribution of ions matches MD results reported earlier (21). Average ionic concentration and equilibrium occupancy along the axis of the channel (z) show features consistent with this pattern (Fig. 4, *A* and *C*), namely, higher concentration of

TABLE 1 Ionic currents and crossing events during BioMOCA simulations of MscS

Structure	Voltage mV	Concentration peri/cyto M	t_{sim} ns	$K^+ \leftarrow$	$K^+ \rightarrow$	$Cl^- \leftarrow$	$Cl^- \rightarrow$	Crossings	Current pA	I_K/I_{Cl}
<i>crystal</i>	0	0.1/0.1	100	0	0	4	4	0	0.0	0.00
<i>crystal</i>	0	0.1/0.1	100	0	0	3	3	0	0.0	0.00
<i>crystal</i>	0	0.1/0.1	100	0	0	4	3	-1	-1.6	0.00
<i>crystal</i>	0	0.1/0.1	100	0	0	1	6	5	8.0	0.00
<i>crystal</i>	+100	0.1/0.1	100	4	0	4	30	30	48.1	0.15
<i>crystal</i>	+100	0.1/0.1	100	1	0	2	25	24	38.5	0.04
<i>crystal</i>	+100	0.1/0.1	100	2	0	1	23	24	38.5	0.09
<i>crystal</i>	-100	0.1/0.1	100	0	0	7	0	-7	-11.2	0.00
<i>crystal</i>	-100	0.1/0.1	100	0	1	9	1	-9	-14.4	0.13
<i>crystal</i>	-100	0.1/0.1	100	0	1	11	2	-10	-16.0	0.11
<i>crystal</i>	+200	0.1/0.1	100	6	0	1	74	79	126.6	0.08
<i>crystal</i>	-200	0.1/0.1	100	0	1	12	0	-13	-20.8	0.08
<i>crystal</i>	0	0.2/0.2	100	0	0	3	5	2	3.2	0.00
<i>crystal</i>	+50	0.2/0.2	100	2	0	4	12	10	16.0	0.25
<i>crystal</i>	-50	0.2/0.2	100	0	1	8	1	-8	-12.8	0.14
<i>crystal</i>	+100	0.2/0.2	100	0	0	2	31	29	46.5	0.00
<i>crystal</i>	-100	0.2/0.2	100	0	0	12	0	-12	-19.2	0.00
<i>crystal*</i>	0	0.2/0.2	90	0	1	4	6	1	1.8	0.50
<i>crystal*</i>	+100	0.2/0.2	100	0	0	2	43	41	65.7	0.00
<i>crystal*</i>	-100	0.2/0.2	90	0	5	12	0	-17	-30.3	0.42
<i>crystalNC</i>	0	0.2/0.2	100	0	0	3	0	-3	-4.8	0.00
<i>crystalNC</i>	+100	0.2/0.2	100	7	0	1	24	30	48.0	0.30
<i>crystalNC</i>	-100	0.2/0.2	100	1	3	10	0	-12	-19.2	0.20
<i>crystalCR</i>	0	0.2/0.2	100	0	1	2	2	-1	-1.6	-
<i>crystalCR</i>	+100	0.2/0.2	100	0	0	0	16	16	25.6	0.00
<i>crystalCR</i>	-100	0.2/0.2	100	0	0	6	0	-6	-9.6	0.00
<i>open1</i>	0	0.1/0.1	100	1	0	21	22	2	3.2	1.00
<i>open1</i>	+50	0.1/0.1	200	3	0	22	65	46	36.9	0.07
<i>open1</i>	+50	0.1/0.1	606	3	0	62	199	140	37.0	0.02
<i>open1</i>	-50	0.1/0.1	200	0	3	51	26	-28	-22.4	0.12
<i>open1</i>	+100	0.1/0.1	100	2	0	10	55	47	75.3	0.04
<i>open1</i>	-100	0.1/0.1	100	0	3	36	2	-37	-59.3	0.09
<i>open1</i>	0	0.2/0.2	100	2	0	22	15	-5	-8.0	0.28
<i>open1</i>	+50	0.2/0.2	100	4	0	12	34	26	41.6	0.18
<i>open1</i>	-50	0.2/0.2	100	2	4	37	8	-31	-49.6	0.07
<i>open1</i>	0	0.3/0.1	200	0	5	29	51	17	13.6	0.23
<i>open1</i>	0	0.1/0.3	200	3	2	55	27	-27	-21.6	0.04
<i>open2</i>	0	0.2/0.2	100	2	3	22	22	-1	-1.6	-
<i>open2</i>	+100	0.2/0.2	100	13	1	6	81	87	139.3	0.16
<i>open2</i>	-100	0.2/0.2	100	3	7	53	9	-48	-76.9	0.09
<i>open3</i>	0	0.2/0.2	100	5	6	40	48	7	11.2	0.13
<i>open3</i>	+100	0.2/0.2	100	23	3	17	124	127	203.4	0.18
<i>open3</i>	-100	0.2/0.2	100	0	5	72	20	-57	-91.3	0.10

Structures are labeled as explained in the text and shown in Fig. 1. The constant bias voltage indicated for each simulation is set at the cytoplasmic boundary of the bath, while the periplasmic boundary is held fixed at 0 V. Ionic concentrations are specified for periplasmic and cytoplasmic boundaries. Ion-crossing events are denoted for each species as \rightarrow for an ion going from the periplasm toward the cytoplasm and \leftarrow for an ion going in the opposite direction.

*Dielectric coefficient in the protein region $\epsilon_p = 20$; see text.

negative ions at the ends of the transmembrane domain and higher concentrations of positive ions at the distal zone of the cytoplasmic domain. Note that the distribution of ions seems to be rather independent of the biasing potential.

Further investigation of MscS's transport properties were carried out with MscS's crystal structure without its cytoplasmic domain (*crystalNC*, residues 27–128) at 0 and ± 100 mV using symmetric baths of 0.2 M KCl. The absence of the cytoplasmic domain resulted in slightly larger ionic currents and decreased selectivity of anions over cations (see Table 1).

All ionic currents monitored in the BioMOCA simulations of MscS in its *crystal* and alternative conformation *crystalNC*

were smaller than experimental values, particularly at negative potentials (see Fig. 5 A). While experimental ionic currents of MscS at -100 mV are close to -100 pA, the ionic currents observed in BioMOCA simulations are -20 pA. Interestingly, ionic currents observed for positive potentials are in better agreement with the experimental values. These currents are in the range of previous estimates (70–250 pS (20,21)). Note, however, that the *crystal* conformation is slightly narrower than the crystal structure itself (see Methods). The simulations also indicate an extremely selective transmembrane pore. BioMOCA simulations of MscS's crystal structure using CHARMM radii instead of

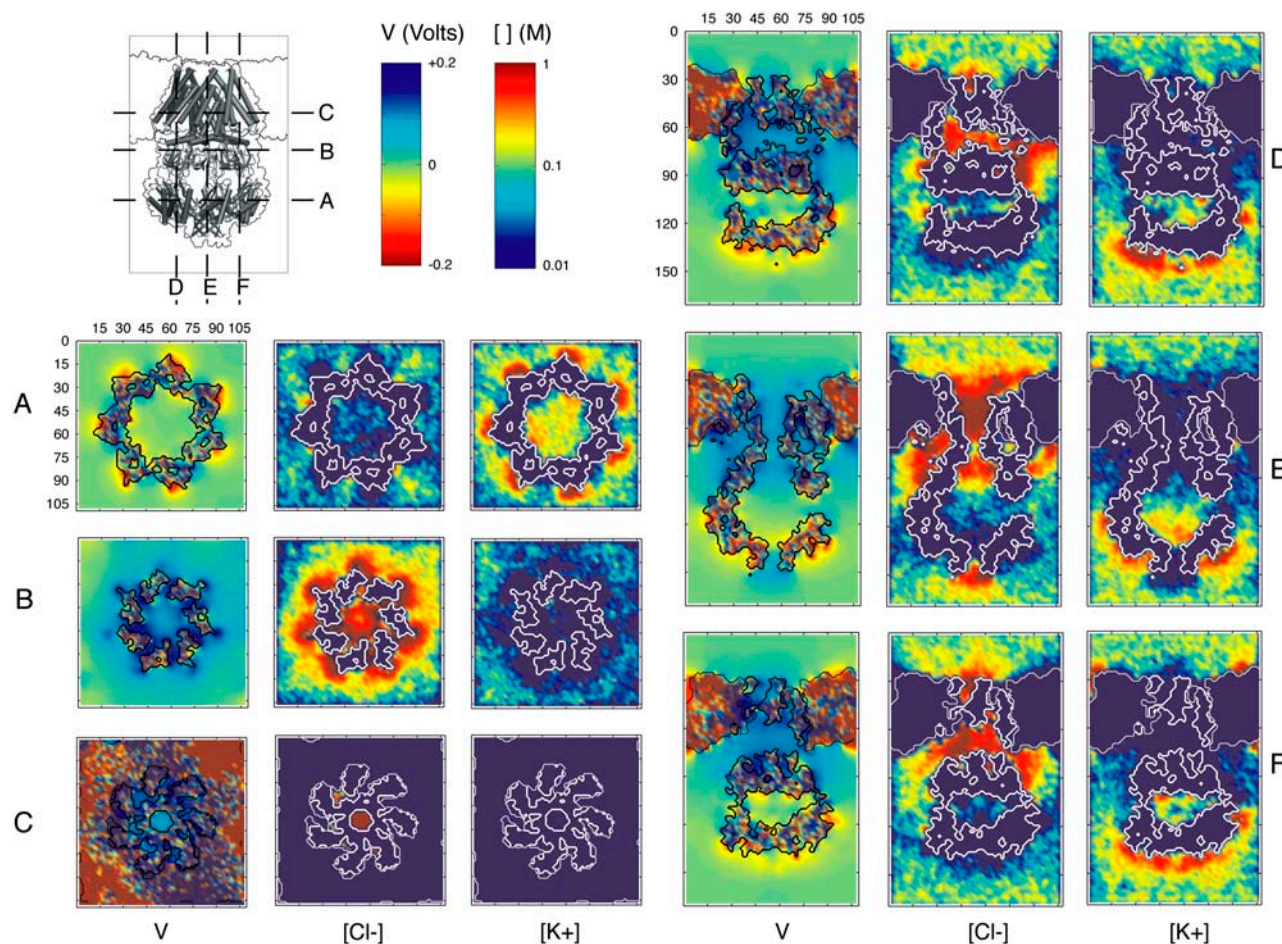


FIGURE 2 Two-dimensional slices through conformation *crystal* of MscS showing the equilibrium (no bias) electrostatic potential along with K^+ and Cl^- concentrations averaged over 100 ns of simulation. Symmetric KCl bath concentrations of 100 mM were used. Concentrations are plotted in moles per liter (M) on a logarithmic scale and potential is plotted in Volts on a linear scale. All values above or below the scale limits are shown at the same level. (A–C) Transverse slices parallel to the membrane, intersecting the transmembrane region as well as the two regions where each ion species tends to congregate exclusively. (D–F) Longitudinal slices in the direction normal to the membrane as indicated in the legend.

VMD radii (*crystalCR*, see Methods and Supplementary Material's Table 3) resulted in even smaller currents and higher selectivity (Table 1), indicating the relevance of the chosen set of radii for the computed MscS's transport properties.

Finally, three test simulations (at 0 and ± 100 mV using symmetric baths of 0.2 M KCl) of the *crystal* conformation were performed using a dielectric constant of $\epsilon_p = 20$ for the protein region. The corresponding currents (Table 1) are similar to those obtained with $\epsilon_p = 5$ (larger in magnitude but still smaller than what is expected for the fully conductive conformation of the channel).

Electrostatic and transport properties of MscS in open conformations

Further BioMOCA simulations were performed on three candidates for the MscS open conformation: *open1* ($r_{\min} =$

3.75 Å), *open2* ($r_{\min} = 5.8$ Å), and *open3* ($r_{\min} = 7.85$ Å, see Methods and Fig. 1). It is interesting to note that all the open conformations featured a less pronounced kink at Gly¹¹³, leading to more straight TM3 helices than those observed in the *crystal* conformation, thereby suggesting a possible gating mechanism (see Supplementary Material's Fig. 7). Since further experimental tests are needed to judge these open conformations, we refrain from further speculation.

BioMOCA simulations of the *open1* conformation revealed an electrostatic pattern similar to that observed for the *crystal* conformation (data not shown). Indeed, average ion concentration and occupancy (Fig. 4, B and D) along the axis of the pore are just slightly different from those observed for the *crystal* conformation. Preliminary studies on MscS homologs show that this pattern seems to be conserved throughout different species as well (L. Kunz, M. Sotomayor, and K. Schulten, unpublished). Currents monitored during simulations without biasing potential were close to zero, as

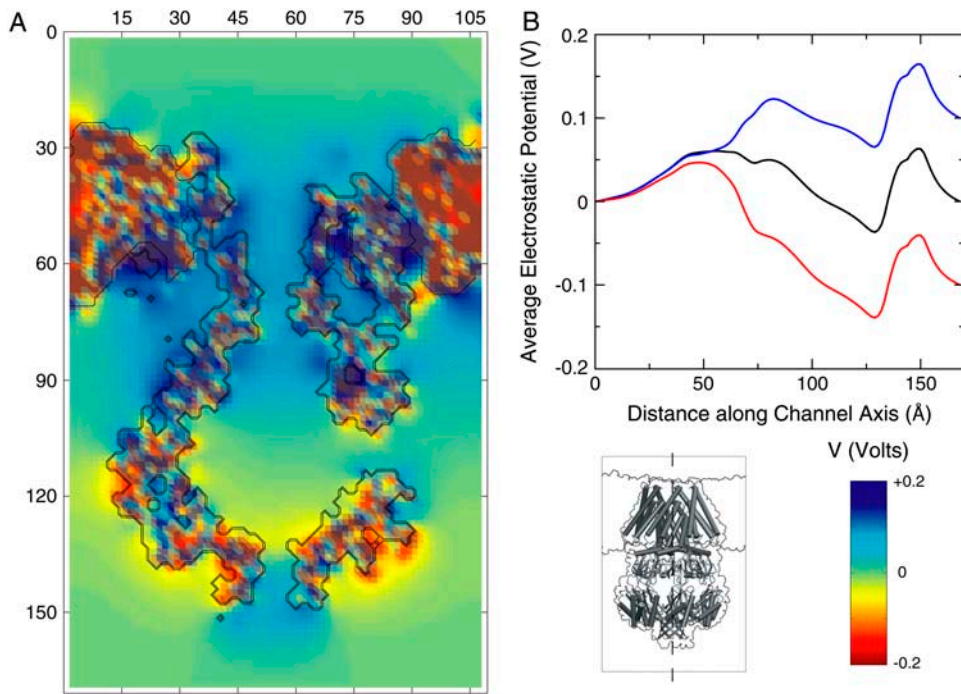


FIGURE 3 Detail of MscS electrostatic potential. (A) Amplified view of equilibrium electrostatic potential as shown in Fig. 2 E. (B) Time-averaged electrostatic potential profile along the channel axis for conformation *crystal* in symmetric 100 mM KCl baths under 0 (black), +100 mV (blue), and -100 mV (red) biasing potentials.

expected, whereas application of a 50 mV biasing potential led to a net ionic current of 37 pA for two simulations lasting 200 and 606 ns (Table 1). When the biasing potential was set to -50 mV the ionic current was found to be -22.4 pA (200 ns); ionic currents in simulations where the biasing potential was set to 100 and -100 mV were found to be 75.3 and -59.3 pA, respectively. The currents are compatible with a conductance slightly lower than 1 nS. Additional simulations performed using symmetric baths of 0.2 M KCl and biasing potentials of 0 and ± 50 mV showed similar results with slightly larger currents and no clear rectification (Table 1). Although the net currents observed for *open1* are in reasonable agreement with those observed experimentally (slightly smaller, particularly for negative potentials), all currents originated from Cl^- ions. Therefore, we further tested selectivity by performing two additional simulations using asymmetric baths of 0.3/0.1 or 0.1/0.3 M KCl. Asymmetric conditions are used in experiments to infer the selectivity of ion channels. A nonselective channel would let both positive and negative ions go down the concentration gradient, thereby generating a zero net current. The ionic currents over 200 ns of simulation under asymmetric conditions were found to be 13.6 and -21.6 pA, mainly driven by Cl^- ions, corroborating the strong selectivity observed in the previous simulations (and indicating that at least at low voltages the channel in the *open1* conformation may favor conduction of ions from the cytoplasm to the periplasm). In contrast, experimental results (2,26) suggest only slight selectivity. Trajectories of ions were visually inspected for one simulation of the *open1* conformation with a biasing potential of

100 mV. Positive and negative ions were found to enter and leave the cytoplasmic domain of MscS through its side openings as previously observed in MD simulations (21), but mainly negative ions passed through MscS's transmembrane pore.

Simulations of the *open2* conformation (see Fig. 1 E) performed using symmetric baths of 0.2 M KCl and external potentials of 0 and ± 100 mV exhibited ionic currents larger than those observed in experiments for positive potentials (see Table 1). Although the number of positive ions crossing the transmembrane domain of MscS was larger than for *crystal* and *open1* conformations, the pore was found again to be highly selective. On the other hand, ionic currents at negative potentials (likely overestimated as discussed below; see Fig. 5 B) are in reasonable agreement with experiments.

BioMOCA simulations of the *open3* conformation, which features the widest transmembrane pore ($r_{\min} = 7.85 \text{ \AA}$, see Fig. 1, D and F), revealed electrostatic patterns similar to those described above, but ionic currents were found to be larger than those calculated for all the other conformations and those reported in experiments at positive potentials. Although the number of positive charges crossing the transmembrane domain is significantly larger than for conformations *crystal*, *open1*, and *open2*, relative currents continue to show strong selectivity, likely because of the presence of Lys¹⁶⁹ at the cytoplasmic end of the transmembrane domain (see Fig. 1 F), and Arg⁸⁸ located at the periplasmic end of the pore, as well as other charged residues around the cytoplasmic side openings.

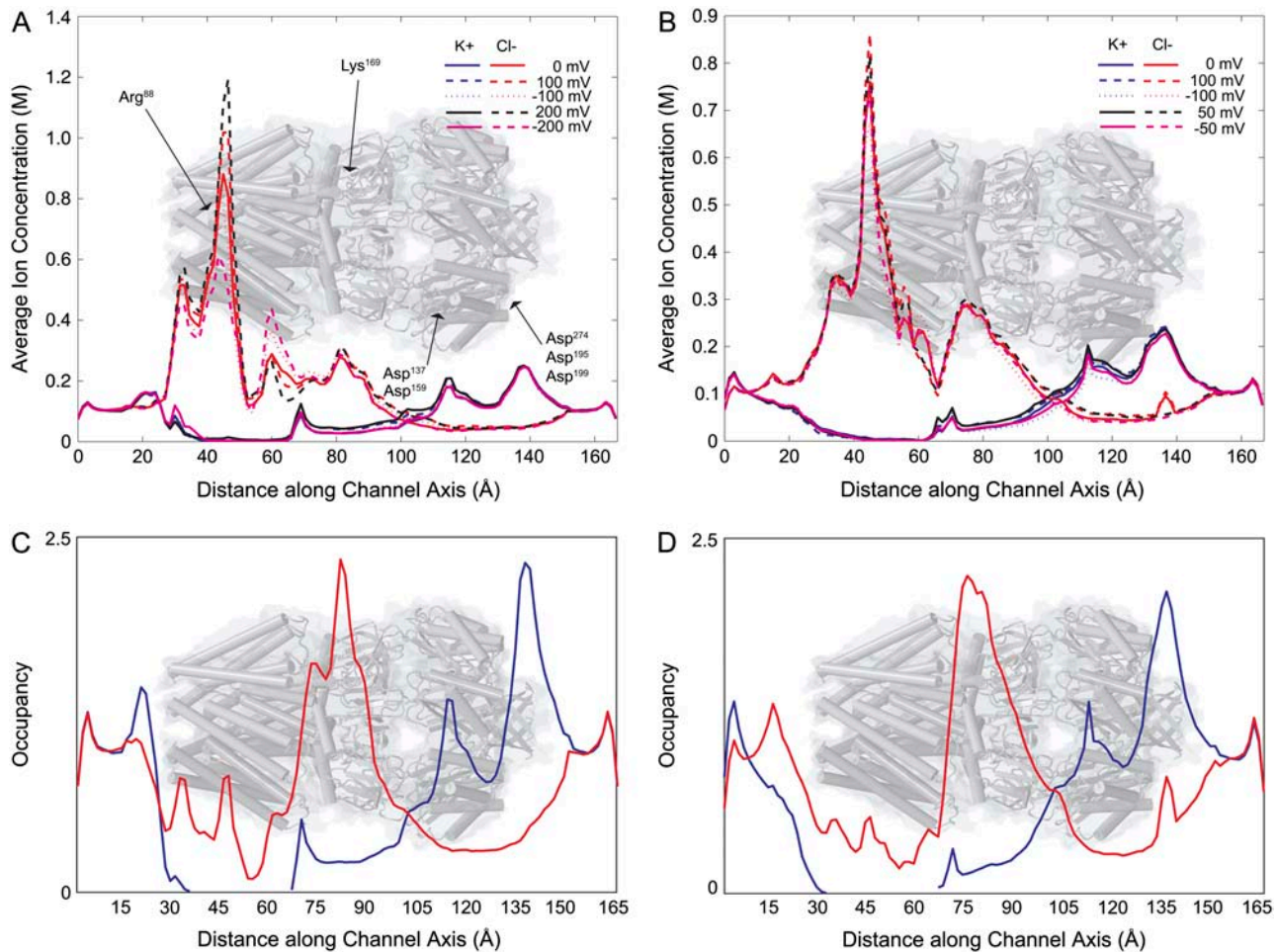


FIGURE 4 Average one-dimensional ion concentration and equilibrium occupancy. (A,B) Average ion concentration profiles for conformations *crystal* and *open1* in symmetric 100 mM KCl baths under different biasing potentials (see legend). The ion concentration profiles were constructed from the time-averaged three-dimensional density maps by integrating the ion density in two-dimensional planes parallel to the membrane and normalizing by the total ion-accessible volume in that plane. (C,D) Equilibrium (no bias) K^+ (blue) and Cl^- (red) occupancy profiles along the channel for conformations *crystal* and *open1* in symmetric 100 mM KCl baths, respectively. The vertical scale indicates the average number of ions found per 1.5 Å slab parallel to the membrane and includes contributions from ions located in aqueous regions both within and outside the channel (see Methods). The approximate location of the channel along with relevant charged residues is indicated in each plot.

Schematic models, selectivity, and rectification

The strong selectivity observed in the simulations of different conformations of MscS led us to design schematic models that could shed light on the origin of this phenomenon. The schematic models consist of an artificial membrane 50 Å thick ($\epsilon = 2$), a cylindrical pore across the center of the membrane with radius 5 Å, and in some cases rings of seven unitary charges placed so as to mimic MscS's charge distribution (see Methods and Fig. 6 A). Snapshots of the time-averaged electrostatic potential and ionic distributions obtained through BioMOCA simulations of schematic models *mod1* and *mod3* are shown in Fig. 6, B and C, respectively. As expected, ionic distributions are uniform for the all-neutral *mod1* model, while negative and positive ions are highly concentrated around the decorating charges placed at the ends of the pore in the *mod3* model. Ionic currents for

each of the simplified models are listed in Table 2. Permeation events over 200 ns were only observed for models *mod2*, *mod3*, and *mod4*, indicating that conduction of ions was triggered by the presence of charges at the ends of the pore. Furthermore, the channel was switched from being completely selective for anions to completely selective for cations by changing the sign of the charges placed at the ends of the pore (see Table 2). A similar behavior has been observed in modified carbon nanotubes simulated explicitly over few nanoseconds (82). A slight difference between the currents driven by positive and negative charges (*mod2* and *mod4*) was observed and is likely caused by the difference in size and diffusion coefficient for K^+ and Cl^- ions. The presence of a third, negatively charged, ring on the cytoplasmic side in the *mod3* model seems to have little impact on the net ionic current computed. Wider models ($r_{\min} = 10$ Å)

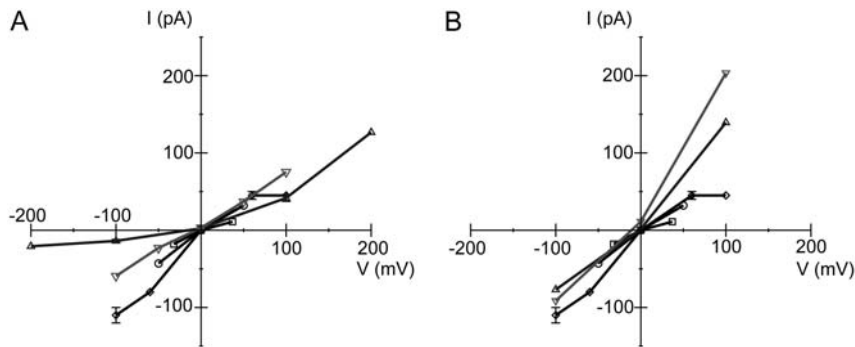


FIGURE 5 Current-voltage curves for different MscS conformations. Single-channel current-voltage curves computed with BioMOCA for (A) conformation *crystal* (Δ) and conformation *open1* (∇) in 100 mM KCl symmetric solution and (B) for conformation *open2* (Δ) and conformation *open3* (∇) in 200 mM KCl symmetric solution. Experimental data adapted from (2) (200 mM KCl, \circ), (26) (100 mM KCl, \square) and (23) (200 mM KCl, \diamond). Experimental curves have not been normalized to the specific buffer conductivity of different experimental setups and, therefore, provide only an approximate reference.

mod5, *mod6*, and *mod7* exhibited a similar behavior (see Table 2). While the all-neutral models *mod5* and *mod7* showed low conductance and low selectivity, the positively charged rings of *mod6* enhanced conductance threefold and induced a high selectivity for anions.

The only model that featured a slight rectification was *mod5* (simulated twice for each voltage, see Table 2), in which a neutral ring of atoms at the cytoplasmic entrance of the channel may have obstructed the passage of ions (steric effect). The rectification due to steric effects seems to be overcome as soon as net charges are assigned to atoms decorating the ends of the channel. While these results certainly do not fully explain MscS's selectivity and rectification, they hint at some specific features of the simulated structure that could be behind the observed behavior: within the assumptions of our models, location of charges near the ends of the channel have a direct influence on selectivity, while steric effects may cause rectification.

The schematic models served as control systems as well. Using Hille's equation (72) one can estimate an upper limit to the resistance R_{channel} of a channel of radius a and length l bathed in a solution of resistivity ρ as

$$R_{\text{channel}} = \left(l + \frac{\pi a}{2} \right) \frac{\rho}{\pi a^2}. \quad (6)$$

If one sets $\rho = 80 \text{ } \Omega\text{cm}$, $l = 50 \text{ } \text{\AA}$ and $a = 10 \text{ } \text{\AA}$ (*mod7*), one obtains $R_{\text{channel}} = 1.67 \text{ G}\Omega$, equivalent to $\sim 598 \text{ pS}$. A pore subject to a 100 mV voltage drop across the membrane should then exhibit a current of $\sim 60 \text{ pA}$, which is larger than the value observed for *mod7* ($\sim 36 \text{ pA}$). Similarly, a pore of radius $a = 5 \text{ } \text{\AA}$ subject to a voltage drop of 100 mV would exhibit a current of $\sim 17 \text{ pA}$. The small value may explain why ionic currents were not observed for simulations of *mod1* over 200 ns. Likely, the pore would exhibit a current smaller than the limit set by Hille's equation, and an even smaller value might be expected due to obstruction effects caused by atoms decorating the ends and cytoplasmic entrance of *mod1*. Such a small current is probably within the limits of what can be observed during 200 ns of simulation (one ion crossing equivalent to $\sim 1 \text{ pA}$). However, control simulations performed on *mod1* using a smaller

radius for decorating atoms and a smaller mesh spacing for the grid did not exhibit permeation events either.

Sources of errors

Among multiple sources of error and approximations of the models presented here, four issues need to be addressed in future simulations and modeling of MscS; a brief discussion about each of them follows.

The first problem that needs to be addressed is the effect of missing residues in the crystallographic structure of MscS. The first 26 residues of the N-termini and the last six residues in the C-termini were not resolved in the crystal structure (11) and, therefore, not included in present and previous (21) simulations. While there is some experimental evidence that the missing domains are not fundamental for MscS function (33,34), details of the electrostatic potential at the C- and N- termini may be influenced by missing charged residues (three negatively charged per subunit at the N-termini; two negatively charged and two positively charged residues per subunit at the C-termini) and the charges of the dissociated termini themselves.

The second issue is related to probable deformations of the MscS structure caused by crystallization conditions. The crystal was solved using a detergent solution that may not represent the hydrophobic membrane environment well. Moreover, the large cytoplasmic domain of MscS participates in multiple lattice contacts. Indeed, each molecule in the unit cell is interacting with two or three other molecules (see Supplementary Material's Fig. 8). While the transmembrane domains do not participate in these lattice contacts, TM1–TM2 loops of different molecules are within $4 \text{ } \text{\AA}$ between each other in some cases (see Supplementary Material's Fig. 8 D), which may explain the unusual tilt of MscS's transmembrane helices. In addition, lattice contacts between different domains of the cytoplasmic domain can directly affect the conformation of TM3 and, thereby, affect the architecture of the pore. Indeed, previous MD simulations showed a displacement of the cytoplasmic domain and the TM3 domain toward the membrane (21). Experiments have also shown that co-solvents can induce changes in the cytoplasmic domain and, thereby, affect MscS gating (32).

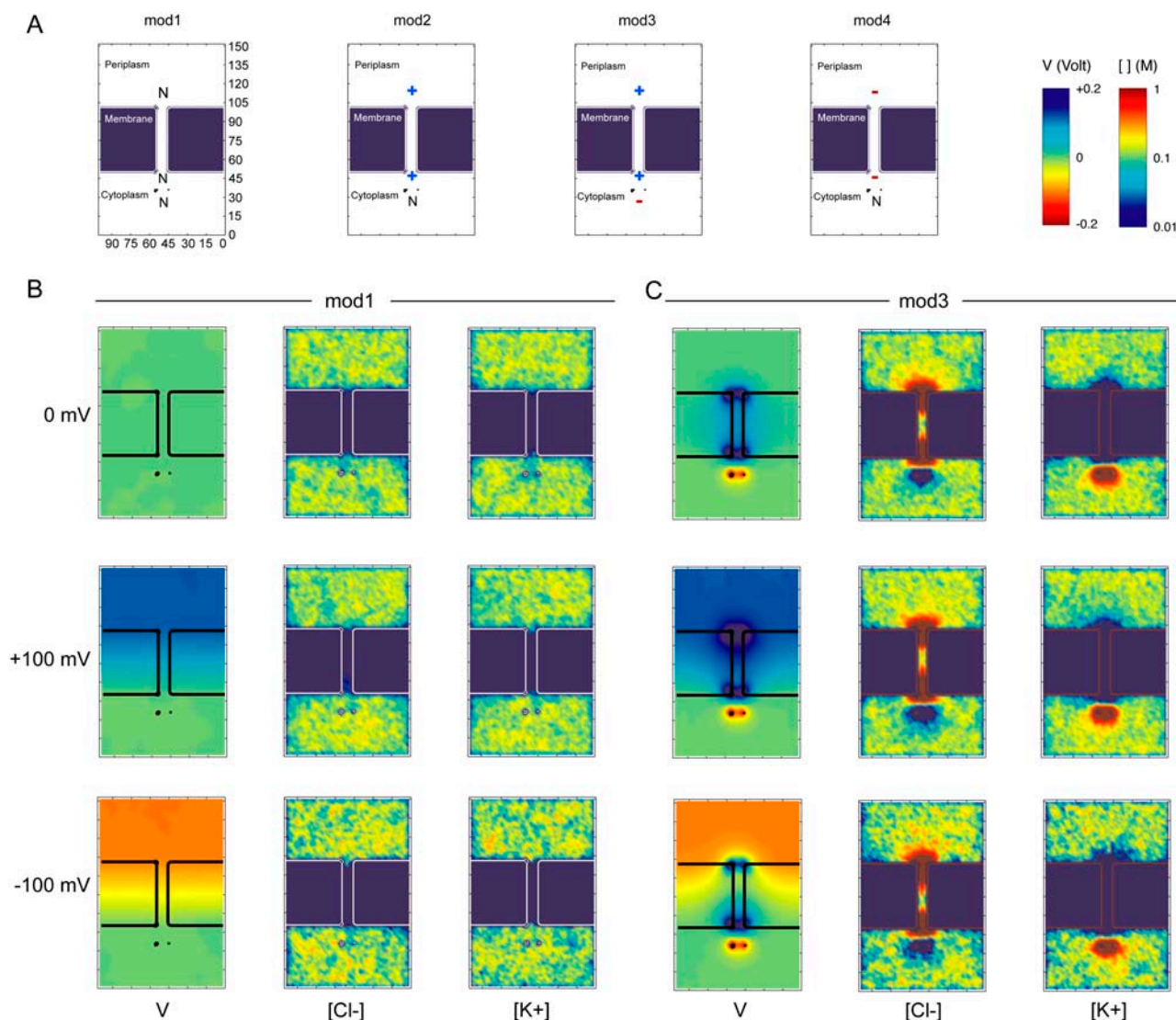


FIGURE 6 Schematic models used to explore the effect of charged residues on channel selectivity and conductance. (A) Geometry of models containing a membrane with a pore of radius 5 Å decorated with three rings of seven atoms each. The rings are located at both ends of the pore and 15 Å away from the membrane in the cytoplasmic side of the bath. Each model (*mod1*, *mod2*, *mod3*, and *mod4*) differs in the charge assigned to these rings of atoms as shown in the figures (neutral atoms are labeled N). (B) Longitudinal slices through *mod1* in the direction normal to the membrane showing the electrostatic potential along with K⁺ and Cl⁻ concentrations averaged over 200 ns for 0 and ±100 mV. Symmetric KCl bath concentrations of 100 mM were used. Concentrations are plotted in moles per liter (M) on a logarithmic scale and potential is plotted in Volts on a linear scale (note that the constant bias voltage indicated is set at the periplasmic boundary for all schematic models, and at the cytoplasmic boundary for all MscS conformations). All values above or below the scale limits are shown at the same level. (C) Longitudinal slices through *mod3* showing the electrostatic potential along with K⁺ and Cl⁻ concentrations averaged over 200 ns as in panel B.

The third problem is related to the intrinsic limitations of the methodology used in the present investigation. The coarse-grained description utilized allowed us to reach timescales of 100 ns or more, but the spatial accuracy of the model is limited. How to best represent the membrane bilayer as a continuum dielectric material (including explicit lipids/hydration water molecules) remains an open question. Furthermore, the dynamics of the protein is not taken into account and, therefore, conformational changes induced by external fields or hydrodynamics effects are ignored. Moreover, ionic

currents presented here represent an upper bound since bulk diffusion constants for ions were used for all regions, even in the narrow transmembrane pore where diffusion of ions may be affected by dewetting transitions and dehydration of ions (not included either in the present model). Smaller diffusion constants would reduce the magnitude of the measured currents without affecting selectivity (70). In addition, changes in the dielectric coefficients and protonation states used for the protein may affect the electrostatic potential and even the strong selectivity observed. Ideally, all-atom simulations could deal

TABLE 2 Ionic currents and crossing events during BiMOCA simulations of different simplified models

Structure	Voltage mV	Concentration peri/cyto M	t_{sim} ns	$\text{K}^+ \leftarrow$	$\text{K}^+ \rightarrow$	$\text{Cl}^- \leftarrow$	$\text{Cl}^- \rightarrow$	Crossings	Current pA	$I_{\text{K}}/I_{\text{Cl}}$
<i>mod1</i>	0	0.1/0.1	200	0	0	0	0	0	0.0	–
<i>mod1</i>	+100	0.1/0.1	200	0	0	0	0	0	0.0	–
<i>mod1</i>	–100	0.1/0.1	200	0	0	0	0	0	0.0	–
<i>mod1*</i>	0	0.1/0.1	100	0	0	0	0	0	0.0	–
<i>mod1*</i>	+100	0.1/0.1	100	0	0	0	0	0	0.0	–
<i>mod1*</i>	–100	0.1/0.1	100	0	0	0	0	0	0.0	–
<i>mod2</i>	0	0.1/0.1	200	0	0	4	3	–1	–0.8	0.00
<i>mod2</i>	+100	0.1/0.1	200	0	0	0	27	27	21.6	0.00
<i>mod2</i>	–100	0.1/0.1	200	0	0	27	1	–26	–20.8	0.00
<i>mod3</i>	0	0.1/0.1	200	0	0	6	6	0	0.0	0.00
<i>mod3</i>	+100	0.1/0.1	200	0	0	0	26	26	20.8	0.00
<i>mod3</i>	–100	0.1/0.1	200	0	0	25	0	–25	–20.0	0.00
<i>mod4</i>	0	0.1/0.1	200	4	5	0	0	–1	–0.8	–
<i>mod4</i>	+100	0.1/0.1	200	18	0	0	0	18	14.4	–
<i>mod4</i>	–100	0.1/0.1	200	3	24	0	0	–21	–16.8	–
<i>mod5</i>	0	0.1/0.1	200	3	4	2	4	1	0.8	0.50
<i>mod5</i>	0	0.1/0.1	170	5	4	6	4	–1	–0.9	0.50
<i>mod5</i>	+100	0.1/0.1	200	24	1	0	29	52	41.6	0.80
<i>mod5</i>	+100	0.1/0.1	200	19	1	0	22	40	32.0	0.80
<i>mod5</i>	–100	0.1/0.1	200	3	16	22	0	–35	–28.0	0.60
<i>mod5</i>	–100	0.1/0.1	127	0	14	11	0	–25	–31.5	1.20
<i>mod5</i>	0	0.1/0.3	200	7	21	2	31	15	12.0	0.50
<i>mod5</i>	0	0.3/0.1	200	21	9	21	6	–3	–2.4	0.60
<i>mod6</i>	0	0.1/0.1	200	0	0	36	39	3	2.4	0.00
<i>mod6</i>	+100	0.1/0.1	200	4	0	1	147	150	120.1	0.03
<i>mod6</i>	–100	0.1/0.1	200	0	3	149	4	–148	–121.7	0.02
<i>mod7</i>	0	0.1/0.1	200	7	6	6	8	3	2.4	0.50
<i>mod7</i>	+100	0.1/0.1	200	24	0	0	22	46	36.9	1.09
<i>mod7</i>	–100	0.1/0.1	200	0	22	24	1	–45	–36.0	0.96

Structures are labeled as explained in the text and shown in Fig. 6. The constant bias voltage indicated for each simulation is set at the periplasmic boundary of the bath, while the cytoplasmic boundary is held fixed at 0 V. Ionic concentrations are specified for periplasmic and cytoplasmic boundaries. Ion-crossing events are denoted for each species as \rightarrow for an ion going from the cytoplasm toward the periplasm and \leftarrow for an ion going in the opposite direction.

*Radius of decorating atoms set to 0.5 Å instead of 1.5 Å; see text.

with these methodological issues; however, with present computer technology, such in situ simulations involving $\sim 225,000$ atoms permits only several simulations of tens of nanoseconds (40), compared to multiple simulations of altogether several microseconds presented here.

Finally, the location and composition of the membrane need to be carefully analyzed. Molecular dynamics simulations, theoretical modeling, and experiments (20,21,33) suggest that the position of the membrane is likely to be slightly different from that suggested in Bass et al. (11), with residues 22–26 immersed in the bilayer. Moreover, the overall positive potential of the transmembrane domain may attract anionic lipids present in *E. coli*. How anionic lipids interact with MscS is unknown, and what the effect of these lipids on selectivity might be, remains to be elucidated. Other bacterial channels are known to depend on anionic lipids to function (83).

CONCLUSIONS

In comparing the results presented in this study with experimental data, we point out first that, although recent

experimental studies have shed light on MscS architecture and function, the complexity of MscS's behavior reveals itself in several contradictions and questions that remain unanswered. Indeed, the channel was originally thought to be a hexamer (26), whereas the structure revealed a heptamer (11). The structure was suggested to represent a fully open conformation of the channel (11), but further studies make it more likely that the *crystal* conformation represents instead a nonconductive state (20,23). However, distances measured from cross-linking of site-specific cysteines in a probable closed state do not correspond well with those observed in the structure (30), suggesting large conformational changes upon gating or inactivation (23). Moreover, the size of the pore, when fully open, remains experimentally undetermined and the in-plane area expansion of the channel was first predicted to be $8.4 \pm 0.4 \text{ nm}^2$ (26), and then estimated to be 18 nm^2 (23). While some studies have reported inactivation (7,23,27,31,32,34), others do not mention it (2,26), and the original voltage dependence for activation of MscS (2) has been challenged in more recent studies (23,27). In addition, the cytoplasmic domain was first characterized as essential for the stability of the protein (33), but now is being

suggested to be nonessential and only responsible for increased stability and activity (34). Finally, the magnitude of ionic currents at relatively small voltages ($> \pm 40$ mV) becomes variable due to an abundance of subconducting states (23) and further evidence of a subconductance state has been recently reported (28) using recording techniques with 3- μ s resolution. Indeed, the conductances reported for MscS vary from 970 pS (650 pS for depolarizing voltages) (2), and 540 pS (270 pS) (26), to 1250 pS (22), likely due to differences in buffer conductivity.

In the context of the experimental results described above, the simulations presented here, although far from conclusive and mainly of qualitative significance, suggest that the crystal structure does not represent the fully open state of MscS. Slightly wider channels are found in our simulations to reproduce the experimentally determined currents. However, the simulations reveal an unexpected rectification at high voltages and a strong selectivity for anions over cations, which is in relative disagreement with several experimental studies showing only slight anionic selectivity. Several issues may cause this disagreement in selectivity, namely, missing residues and charged N-termini, protonation states of charged residues, or large conformational changes of the structure upon application of tension or voltage. While the crystal structure could represent an inactive state in which the TM3 helices are detached from helices TM1–TM2, which interact with the membrane (20,23), contacts of TM1–TM2 loops with the end of TM3 helices at the cytoplasm (observed in the present and previous studies (21)) may couple TM3 with external helices and membrane. Indeed, forces applied to the end of TM3 helices are required to widen the channel (data not shown), for which TM3 exhibits a less pronounced kink.

The role of the cytoplasmic domain remains unknown, but the simulations presented here indicate that it has a strong influence on the distribution of ions and perhaps on the selectivity of the channel, while its side openings can readily conduct ions. An interesting possibility is that the cytoplasmic domain could act as a molecular sieve (11). Multiple and functional side openings, like the ones observed in this study, seem to give further support to this hypothesis. Upon osmotic shock and exocytosis, these openings would preclude the blockage of the main transmembrane pore by large solutes, and would provide alternative exit pathways for small solutes. Since the main anion in bacterial cells is glutamate (84) and not Cl^- (utilized in patch-clamp experiments), it would be interesting to investigate glutamate's interactions and possible pathways through MscS. Another possible role of the cytoplasmic domain may be related to its influence on gating. Further simulations of the entire (including missing residues and charged termini) MscS channel using different co-solvents may clarify how the cytoplasmic domain dynamics and interaction with intracellular elements could gate the channel and, thereby, provide a sensor for cytoplasmic crowding.

SUPPLEMENTARY MATERIAL

An online supplement to this article can be found by visiting BJ Online at <http://www.biophysj.org>.

We thank Valeria Vasquez, Gulzar A. Kathawala, Barry Isralewitz, Lothar Kunz, and members of the Theoretical and Computational Biophysics Group for helpful discussions. The molecular images in this article were created with the molecular graphics program VMD (85).

This work was supported by the National Institutes of Health (NIH grant No. P41 RR05969, NIH grant No. 1 RO1 GM067887, and NIH grant No. R01-GM073655), by the National Science Foundation (Network for Computational Nanotechnology grant No. EEC-0228390), and by the National Center for Supercomputing Applications. The authors also acknowledge computer time provided by the National Science Foundation (National Resource Allocation committee grant No. MCA93S028).

REFERENCES

- Guharay, F., and F. Sachs. 1984. Stretch-activated single ion channel currents in tissue-cultured embryonic chick skeletal muscle. *J. Physiol.* 352:685–701.
- Martinac, B., M. Buechner, A. H. Delcour, J. Adler, and C. Kung. 1987. Pressure-sensitive ion channel in *Escherichia coli*. *Proc. Natl. Acad. Sci. USA.* 84:2297–2301.
- Sachs, F., and C. Morris. 1998. Mechanosensitive ion channels in non-specialized cells. In *Reviews of Physiology and Biochemistry and Pharmacology*. M. Blaustein, R. Greger, H. Grunicke, R. Jahn, L. Mendell, A. Miyajima, D. Pette, G. Schultz, and M. Schweiger, editors. Springer-Verlag, Berlin, Germany. 1–78.
- Hamill, O. P., and B. Martinac. 2001. Molecular basis of mechanotransduction in living cells. *Physiol. Rev.* 81:685–740.
- Sukharev, S., and D. P. Corey. 2004. Mechanosensitive channels: multiplicity of families and gating paradigms. *Sci. STKE.* 219:Re4.
- Berrier, C., A. Coulombe, I. Szabo, M. Zoratti, and A. Ghazi. 1992. Gadolinium ion inhibits loss of metabolites induced by osmotic shock and large stretch-activated channels in bacteria. *Eur. J. Biochem.* 206:559–565.
- Levina, N., S. Totemeyer, N. R. Stokes, P. Louis, M. A. Jones, and I. Booth. 1999. Protection of *Escherichia coli* cells against extreme turgor by activation of MscS and MscL mechanosensitive channels: identification of genes required for MscS activity. *EMBO J.* 18:1730–1737.
- Blount, P., and P. C. Moe. 1999. Bacterial mechanosensitive channels: integrating physiology, structure and function. *Trends Microbiol.* 18:420–424.
- Sukharev, S. I., P. Blount, B. Martinac, F. R. Blattner, and C. Kung. 1994. A large-conductance mechanosensitive channel in *E. coli* encoded by MscL alone. *Nature.* 368:265–268.
- Chang, G., R. H. Spencer, A. T. Lee, M. T. Barclay, and D. C. Rees. 1998. Structure of the MscL homolog from *Mycobacterium tuberculosis*: a gated mechanosensitive ion channel. *Science.* 282:2220–2226.
- Bass, R. B., P. Strop, M. Barclay, and D. C. Rees. 2002. Crystal structure of *Escherichia coli* MscS, a voltage-modulated and mechanosensitive channel. *Science.* 298:1582–1587.
- Sukharev, S., M. Betanzos, C.-S. Chiang, and H. R. Guy. 2001. The gating mechanism of the large mechanosensitive channel MscL. *Nature.* 409:720–724.
- Gullingsrud, J., D. Kosztin, and K. Schulten. 2001. Structural determinants of MscL gating studied by molecular dynamics simulations. *Biophys. J.* 80:2074–2081.
- Betanzos, M., C.-S. Chiang, H. R. Guy, and S. Sukharev. 2002. A large iris-like expansion of a mechanosensitive channel protein induced by membrane tension. *Nat. Struct. Biol.* 9:704–710.
- Perozo, E., A. Kloda, D. M. Cortes, and B. Martinac. 2002. Physical principles underlying the transduction of bilayer deformation forces during mechanosensitive channel gating. *Nat. Struct. Biol.* 9:696–703.

16. Perozo, E., D. M. Cortes, P. Sompornpisut, A. Kloda, and B. Martinac. 2002. Open channel structure of MscL and the gating mechanism of mechanosensitive channels. *Nature*. 418:942–948.
17. Kong, Y., Y. Shen, T. E. Warth, and J. Ma. 2002. Conformational pathways in the gating of *Escherichia coli* mechanosensitive channel. *Proc. Natl. Acad. Sci. USA*. 99:5999–6004.
18. Gullingsrud, J., and K. Schulten. 2003. Gating of MscL studied by steered molecular dynamics. *Biophys. J.* 85:2087–2099.
19. Colombo, G., S. J. Marrink, and A. E. Mark. 2003. Simulation of MscL gating in a bilayer under stress. *Biophys. J.* 84:2331–2337.
20. Anishkin, A., and S. Sukharev. 2004. Water dynamics and dewetting transitions in the small mechanosensitive channel MscS. *Biophys. J.* 86:2883–2895.
21. Sotomayor, M., and K. Schulten. 2004. Molecular dynamics study of gating in the mechanosensitive channel of small conductance MscS. *Biophys. J.* 87:3050–3065.
22. Edwards, M. D., Y. Li, S. Miller, W. Barlett, S. Black, S. Dennison, I. Iscla, P. Blount, J. U. Bowie, and I. R. Booth. 2005. Pivotal role of the glycine-rich TM3 helix in gating the MscS mechanosensitive channel. *Nat. Struct. Mol. Biol.* 12:113–119.
23. Akitake, B., A. Anishkin, and S. Sukharev. 2005. The dashpot mechanism of stretch-dependent gating in MscS. *J. Gen. Physiol.* 125:143–154.
24. Anishkin, A., and S. Sukharev. 2005. Explicit channel conductance: can it be computed? *Biophys. J.* 88:3742–3743.
25. Martinac, B. 2005. Structural plasticity in MS channels. *Nat. Struct. Mol. Biol.* 12:104–105.
26. Sukharev, S. 2002. Purification of the small mechanosensitive channel of *Escherichia coli* (MscS): the subunit structure, conduction, and gating characteristics in liposomes. *Biophys. J.* 83:290–298.
27. Vasquez, V., and E. Perozo. 2004. Voltage-dependent gating in MscS. *Biophys. J.* 86:545A.
28. Shapovalov, G., and H. A. Lester. 2004. Gating transitions in bacterial ion channels measured at 3 μ s resolution. *J. Gen. Physiol.* 124:151–161.
29. Spronk, S., D. Dougherty, and H. Lester. 2005. Hydration of the pore of the mechanosensitive channel of small conductance (MscS) studied by molecular dynamics. *Biophys. J.* 88:149A.
30. Miller, S., M. D. Edwards, C. Ozdemir, and I. R. Booth. 2003. The closed structure of the MscS mechanosensitive channel. *J. Biol. Chem.* 278:32246–32250.
31. Koprowski, P., and A. Kubalski. 2003. C-termini of the *Escherichia coli* mechanosensitive ion channel (MscS) move apart upon the channel opening. *J. Biol. Chem.* 278:11237–11245.
32. Grajkowski, W., A. Kubalski, and P. Koprowski. 2005. Surface changes of the mechanosensitive channel MscS upon its activation, inactivation, and closing. *Biophys. J.* 88:3050–3059.
33. Miller, S., W. Bartlett, S. Chandrasekaran, S. Simpson, M. Edwards, and I. R. Booth. 2003. Domain organization of the MscS mechanosensitive channel of *Escherichia coli*. *EMBO J.* 22:36–46.
34. Schumann, U., M. D. Edwards, C. Li, and I. R. Booth. 2004. The conserved carboxy-terminus of the MscS mechanosensitive channel is not essential but increases stability and activity. *FEBS Lett.* 572:233–237.
35. Roux, B., and M. Karplus. 1991. Ion transport in a model gramicidin channel. Structure and thermodynamics. *Biophys. J.* 59:961–981.
36. Tieleman, D. P., P. C. Biggin, G. R. Smith, and M. S. P. Sansom. 2001. Simulation approaches to ion channel structure-function relationships. *Q. Rev. Biophys.* 34:473–561.
37. Schlick, T. 2002. *Molecular Modeling and Simulation: An Interdisciplinary Guide*. Springer-Verlag, New York.
38. Roux, B., T. Allen, S. Bernèche, and W. Im. 2004. Theoretical and computational models of biological ion channels. *Q. Rev. Biophys.* 37:15–103.
39. Gumbart, J., Y. Wang, A. Aksimentiev, E. Tajkhorshid, and K. Schulten. 2005. Molecular dynamics simulations of proteins in lipid bilayers. *Curr. Opin. Struct. Biol.* 15:423–431.
40. Aksimentiev, A., and K. Schulten. 2005. Imaging α -hemolysin with molecular dynamics: ionic conductance, osmotic permeability and the electrostatic potential map. *Biophys. J.* 88:3745–3761.
41. Barcilon, V. 1992. Ion flow through narrow membrane channels: Part I. *SIAM J. Appl. Math.* 52:1391–1404.
42. Barcilon, V., D. P. Chen, and R. S. Eisenberg. 1992. Ion flow through narrow membrane channels: Part II. *SIAM J. Appl. Math.* 52:1405–1425.
43. Kurnikova, M. G., R. D. Coalson, P. Graf, and A. Nitzan. 1999. Relaxation algorithm for 3-D Poisson-Nernst-Planck theory with application to ion transport through the Gramicidin A channel. *Biophys. J.* 76:642–656.
44. Cardenas, A. E., R. D. Coalson, and M. G. Kurnikova. 2000. Three-dimensional Poisson-Nernst-Planck studies. Influence of membrane electrostatics on Gramicidin A channel conductance. *Biophys. J.* 79:80–93.
45. Chen, D. P., J. Lear, and R. S. Eisenberg. 1997. Permeation through an open channel. Poisson-Nernst-Planck theory of a synthetic ionic channel. *Biophys. J.* 72:97–116.
46. Eisenberg, R. S. 1996. Computing the field in proteins and channels. *J. Membr. Biol.* 150:1–25.
47. Hollerbach, U., D.-P. Chen, D. D. Busath, and R. S. Eisenberg. 2000. Predicting function from structure using the Poisson-Nernst-Planck equations: sodium current in the Gramicidin A channel. *Langmuir*. 16:5509–5514.
48. Hollerbach, U., D.-P. Chen, and R. S. Eisenberg. 2001. Two- and three-dimensional Poisson-Nernst-Planck simulations of current flow through Gramicidin-A. *J. Sci. Comput.* 16:373–409.
49. Schuss, Z., B. Nadler, and R. S. Eisenberg. 2001. Derivation of PNP equations in bath and channel from a molecular model. *Phys. Rev. E*. 64:036116-1–14.
50. van der Straaten, T. A., J. M. Tang, R. S. Eisenberg, U. Ravaioli, and N. Aluru. 2002. Three-dimensional continuum simulations of ion transport through biological ion channels: effect of charge distribution in the constriction region of porin. *J. Comput. Electron.* 1:335–340.
51. Im, W., and B. Roux. 2002. Ion permeation and selectivity of OmpF porin: a theoretical study based on molecular dynamics, Brownian dynamics, and continuum electrodiffusion theory. *J. Mol. Biol.* 322:851–869.
52. Eisenberg, R. S. 1999. From structure to function in open ionic channels. *J. Membr. Biol.* 171:1–24.
53. Corry, B., S. Kuyucak, and S.-H. Chung. 2000. Tests of continuum theories as models of ion channels. II. Poisson-Nernst-Planck theory versus Brownian dynamics. *Biophys. J.* 78:2364–2381.
54. Noskov, S. Y., W. Im, and B. Roux. 2004. Ion permeation through the α -hemolysin channel: theoretical studies based on Brownian dynamics and Poisson-Nernst-Planck electrodiffusion theory. *Biophys. J.* 87:2299–2309.
55. van der Straaten, T. A., G. Kathawala, A. Trellakis, R. S. Eisenberg, and U. Ravaioli. 2005. BioMOCA—a Boltzmann transport Monte Carlo model for ion channel simulation. *Mol. Sim.* 31:151–171.
56. Jacoboni, C., and P. Lugli. 1989. *The Monte Carlo Method for Semiconductor Device Simulation*. Springer-Verlag, New York.
57. Hockney, R. W., and J. W. Eastwood. 1981. *Computer Simulation Using Particles*. McGraw-Hill, New York.
58. Phillips, J. C., R. Braun, W. Wang, J. Gumbart, E. Tajkhorshid, E. Villa, C. Chipot, R. D. Skeel, L. Kale, and K. Schulten. 2005. Scalable molecular dynamics with NAMD. *J. Comput. Chem.* 26:1781–1802.
59. Smart, O. S., J. G. Neduveilil, X. Wang, B. A. Wallace, and M. S. P. Sansom. 1996. HOLE: a program for the analysis of the pore dimensions of ion channel structural models. *J. Mol. Graph.* 14:354–360.
60. Zhou, F., and K. Schulten. 1995. Molecular dynamics study of a membrane-water interface. *J. Phys. Chem.* 99:2194–2208.
61. MacKerell Jr., A. D., D. Bashford, M. Bellott, R. L. Dunbrack Jr., J. Evanseck, M. J. Field, S. Fischer, J. Gao, H. Guo, S. Ha, D. Joseph, L.

- Kuchnir, et al. 1998. All-hydrogen empirical potential for molecular modeling and dynamics studies of proteins using the CHARMM22 force field. *Journal of Physical Chemistry B*. 102:3586–3616.
62. Nina, M., D. Beglov, and B. Roux. 1997. Atomic radii for continuum electrostatics calculations based on molecular dynamics free energy simulations. *J. Phys. Chem. B*. 101:5239–5248.
63. Nina, M., W. Im, and B. Roux. 1999. Optimized atomic radii for protein continuum electrostatics solvation forces. *Biophys. Chem.* 78:89–96.
64. Im, W., S. Seefeld, and B. Roux. 2000. A grand canonical Monte Carlo-Brownian dynamics algorithm for simulating ion channels. *Biophys. J.* 79:788–801.
65. Sitkoff, D., K. A. Sharp, and B. Honig. 1994. Accurate calculation of hydration free energies using macroscopic solvent models. *J. Phys. Chem.* 98:1978–1988.
66. Baker, N. A., D. Sept, M. J. Holst, and J. A. McCammon. 2001. The adaptive multilevel finite element solution of the Poisson-Boltzmann equation on massively parallel computers. *IBM J. Res. Develop.* 45:427–438.
67. Ashcroft, N. W. and N. D. Mermin. 1976. *Solid State Physics*. W. B. Saunders, Philadelphia, PA.
68. Lide, D. R., editor. 1994. *CRC Handbook of Chemistry and Physics*, 75th Ed. CRC Press, Boca Raton, FL.
69. Allen, T. W., S. Kuyucak, and S. H. Chung. 1999. The effect of hydrophobic and hydrophilic channel walls on the structure and diffusion of water and ions. *J. Chem. Phys.* 111:7985–7999.
70. Smith, G. R., and M. S. P. Sansom. 1999. Effective diffusion coefficients of K^+ and Cl^- ions in ion channel models. *Biophys. Chem.* 79:129–151.
71. Golub, G., and C. van Loan. 1996. *Matrix Computations*, 3rd Ed. The Johns Hopkins University Press, Baltimore and London.
72. Hille, B. 2001. *Ionic Channels of Excitable Membranes*, 3rd Ed. Sinauer Associates, Sunderland, MA.
73. Schutz, C. N., and A. Warshel. 2001. What are the dielectric “constants” of proteins and how to validate electrostatic models? *Proteins*. 44:400–417.
74. Roux, B., and K. Schulten. 2004. Computational studies of membrane channels. *Structure*. 12:1343–1351.
75. Sansom, M. S., G. R. Smith, C. Adcock, and P. C. Biggin. 1997. The dielectric properties of water within model transbilayer pores. *Biophys. J.* 73:2404–2415.
76. Li, S. C., M. Hoyles, S. Kuyucak, and S. H. Chung. 1998. Brownian dynamics study of ion transport in the vestibule of membrane channels. *Biophys. J.* 74:37–47.
77. Chung, S. H., M. Hoyles, T. W. Allen, and S. Kuyucak. 1998. Study of ionic currents across a model membrane channel using Brownian dynamics. *Biophys. J.* 75:793–809.
78. Schirmer, T., and P. S. Phale. 1999. Brownian dynamics simulation of ion flow through porin channels. *J. Mol. Biol.* 294:1159–1167.
79. Sakmann, B., and E. Neher. 1995. *Single Channel Recording*, 2nd Ed. Plenum, New York.
80. van der Straaten, T. A., J. M. Tang, U. Ravaioli, R. S. Eisenberg, and N. Aluru. 2003. Simulating ion permeation through the OmpF Porin ion channel using three-dimensional drift-diffusion theory. *J. Comput. Electron.* 2:29–47.
81. Nonner, W., A. Peyser, D. Gillespie, and B. Eisenberg. 2004. Relating microscopic charge movement to macroscopic currents: the Ramo-Shockley theorem applied to ion channels. *Biophys. J.* 87:3716–3722.
82. Joseph, S., R. J. Mashl, E. Jakobsson, and N. R. Aluru. 2003. Electrolytic transport in modified carbon nanotubes. *Nano. Letters*. 3:1399–1403.
83. Sansom, M., P. Bond, S. Deol, A. Grottesi, S. Haider, and Z. Sands. 2005. Molecular simulations and lipid-protein interactions: potassium channels and other membrane proteins. *Biochem. Soc. Trans.* 33: 916–920.
84. Booth, I. R., M. D. Edwards, E. Murray, and S. Miller. 2005. The role of bacterial channels in cell physiology. *In Bacterial Ion Channels and Their Eukaryotic Homologs*. A. Kubalski and B. Martinac, editors. ASM Press, Washington, DC. 291–312.
85. Humphrey, W., A. Dalke, and K. Schulten. 1996. VMD—visual molecular dynamics. *J. Mol. Graphics*. 14:33–38.